EXPLORATION OF CROCONIC ACID DISODIUM SALT AS AN ORGANIC BATTERY ELECTRODE MATERIAL

by

RUPALI CHAWLA

A Dissertation submitted to the

Graduate School-Newark

Rutgers, The State University of New Jersey

in partial fulfillment of the requirements

for the degree of Master of Chemistry

Graduate Program in

written under the direction of

Prof. Elena Galoppini

and approved by

_____

_____

_____

Newark, New Jersey

January 2019

Abstract

We investigated croconic acid disodium salt for potential use as Li-ion battery material. The crystal was shown to be a promising electrode material with a medium to short battery cycle lifetime. We embarked in a thorough computational study based on classical molecular dynamics simulations to characterize this system and identify optimization strategies to improve battery lifetime. Through long-timescale molecular dynamics simulations in the Canonical Ensemble and Isothermal-Isobaric ensembles, we first established that the custom force field that we generated for this system reproduces the known thermodynamics of the Croconic acid disodium salt dihydrate crystal. In a second step, we predict the existence of a quasi-degenerate denser polymorph which is slightly less stable at room temperature and becomes more stable starting T=420K compared to the known crystal structure as determined by X-Ray crystallography. Interestingly, we find that upon adding lithium the system chooses the denser phase even at room temperature. Lithiation of the denser phase leads to moderate volume increases of about 0.75% for each additional 1% lithiation. By extrapolation of the results of the simulations, we conjecture that a phase transition takes place in the very first stages of lithiation. This should initially reduce the volume, resulting in the formation of cracks in the material contributing to a short battery cycle lifetime. We thus propose to assemble batteries based on croconate at an elevated temperature.

Acknowledgements

I am indebted to my parents and my brother for their unconditional support throughout the course of my education. A special thanks to Prof. Elena Galoppini for guiding me through writing the thesis. I would also like to thank my thesis committee members Prof. Galoppini, Prof. Lockard and Prof. Dias for their time and insightful comments on the thesis. I would also like to thank Prof. Michele Pavanello for giving me an opportunity to work on this project and for all the support and guidance he offered throughout my time in PRG lab.

I want to express my gratitude to my friends here in the US and abroad for standing by me through thick and thins. A special thanks to my roommates for making a hard day just a little bit easier.

I would like to thank the chemistry department at Rutgers University for giving me the opportunity to present my work in the form of dissertation. A special thanks to the CBET-NSF for the financial support offered for this project. I also acknowledge the support of NM3 computing facility at Rutgers University, Newark, New Jersey.

Contents

1 Introduction **1**

1.1 Introduction to Battery Materials 1

1.2 Croconic Acid Disodium Salt - Electrode Material 5

1.3 Molecular Mechanics 7

2 Exploration of CADS Crystal **10**

2.1 Crystal Structure Information 10

2.2 Molecular Dynamics 11

2.3 Force Field Optimization 13

2.3.1 Computational Details 13

2.3.2 Results and discussion 15

2.4 Selection of τ-Pressure for barostat 23

2.4.1 Computational Details 24

2.4.2 Results and Discussion 24

2.5 Heating of CADS Crystal 25

2.5.1 Effects over Volume of the Battery 26

2.5.2 Thermodynamic Analysis of Crystal Structure 26

3 Charging of the CADS Crystal with Lithium **31**

3.1 Computational Details 32

3.2 Results and Discussion 32

4 RMSD Analysis **35**

5 Conclusion **40**

A Sample of a .Key file **42**

B Customized OPLS-AA force field **44**

Chapter 1

Introduction

1.1 Introduction to Battery Materials

Global warming is posing a serious threat due to increasing consumption of fossil fuels and other non renewable energy sources. In the recent years, emphasis is being laid on production of green energy from renewable energy sources like sun, wind and water. There have been many efforts to replace combustion engines with hybrid vehicles, plugin hybrid vehicles and full electric vehicles.[1] A significant contribution has been made towards ecological sustenance by electrifying automobiles and replacing gasoline with more environment friendly fuels. The exploitation of these green energy sources in lieu of fossil fuels, requires an incessant exploration of environment friendly green energy storage devices.[2] Electrochemical batteries are currently the most promising candidates for such storage devices.[3, 4] These batteries provide portability, stored chemical energy as well as ability of converting the stored energy into electrical energy.

Rechargeable batteries are a type of electrochemical batteries that were first introduced in 1859 by French physician, Gaston Planté. Due to environmental benefits,

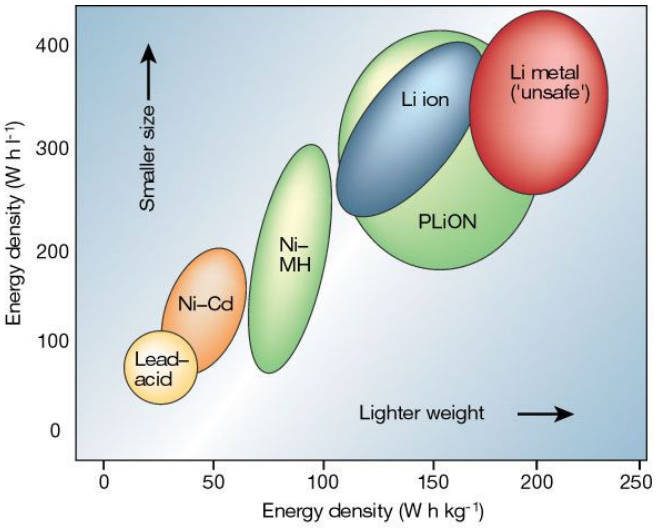

Figure 1.1: Comparison of different rechargeable batteries in terms of volumetric and gravimetric densities[9]

low costs and high lifetime, rechargeable batteries are much more in demand than other kind of electrochemical batteries. Early developments in rechargeable batteries include Lead acid, Nickel-Cadmium, Nickel-Iron, Zinc-Carbon batteries among others. Lithium Ion Batteries (LIBs) are one such popular type of rechargeable batteries. Along with Lithium, other metal ion batteries such as Sodium, Magnesium and Aluminium ion batteries are being extensively studied.[5–8] Due to their small size and the ease of transportation of these ions make them an ideal charge carriers for the batteries.

Among these new gen electrochemical batteries, LIBs are considered most promising due to their high specific energy, high rate capability, high safety and low cost.[2, 3, 9–11]. Lithium has a higher gravimetric capacity, which is critical in portable electronics, gives LIBs an edge over other metal ion based batteries.[11] Figure 1.1 compares volumetric and gravimetric densities of different batteries. The worldwide sales of LIBs exceed at least by a factor of 2.5 in comparison to any other competing battery technology due to the high value of gavimetric energy density of 150 $Whkg^{-1}$.[9] and volumetric energy density of 650 Whl^{-1}. Today, LIBs are the key to revolutionizing

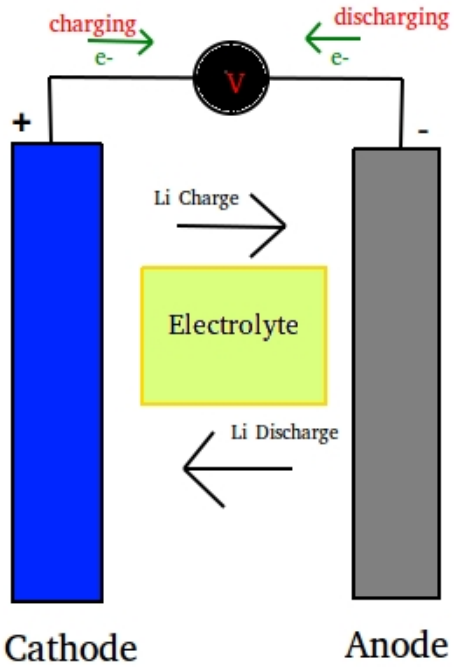

Figure 1.2: Schematic diagram of a LIBs indicating the direction Li ions and electrons take while charging and discharging

portable electronic materials.

Key components of LIBs are cathode, anode and electrolyte/separator. A schematic of a battery is shown in figure 1.2. The anode (also known as the negative electrode), is made of Carbon in conventional rechargeable LIBs, cathode is made usually with an inorganic compound of Lithium and electrolyte is usually a liquid or a dry polymer solid. Among this, cathodes are most extensively studied as high voltage of cathode materials can improve the power densities of LIBs. Cathodes with higher rate capability, higher charge capacity, and for cathodes sufficiently high voltage can improve the energy and power densities of Li batteries and make them smaller and cheaper. Cathode comprising of Lithium and transition metal oxides of the form Li_xMo_2 (M = Co, Ni, Mn) are most commonly used as cathodes.[3, 12] Transition metal oxides are still considerably favored due to their variable valence states.[2, 12]

However, the extraction process and usage of these metals is an expensive process and produces heavy metal waste.[13] In addition to being environmental hazard, the capacity of a typical cathode material like $LiCoO_2$ and $LiFePO_4$ is about 150 $Ahkg^{-1}$, which does not yet meet the energy density required by Electrochemical Vehicles.[9, 14] Hence there is a strong need for electrode materials that can be produced at low cost and are environmentally benign.

In light of all these challenges, one possible solution that is being currently explored, is to make LIBs electrodes with organic compounds. Metal-organic Frameworks (MOFs) are being actively studied and synthesized as electrodes to provide a porous framework in Li ion battery materials.[15] With their huge surface area, low density and high porosity, MOFs could be potentially used for LIBs. Several MOFs such as ZIF-8, ZIF-67, Uio-66 and MIL-101 have been designed as electrode materials for LIBs. However, they come with their own set of challenges including low conductivity and chemical stability. [14]

Conjugated carbonyl derivatives are recently getting much attention as potential electrode materials. Compounds such as purpurin, 3,4,9,10-perylene-tetracarboxylicacid-dianhydride (PTCDA), polyimides, tribrominated trioxotrangulene among others are categorised under ”green-battery” materials.[16–21] However, the stability and charging/discharging of these organic battery materials makes it challenging to convert them into potential electrodes that can meet the high energy demands of modern society. Studies are still being carried out to improve their electrical conductivity when compared to their inorganic counterparts.[14] Many groups have analyzed organic electrodes for potential battery materials. There have been theoretical and synthetic studies concerning the charging/discharging of the batteries, band gap studies as well as calcu-

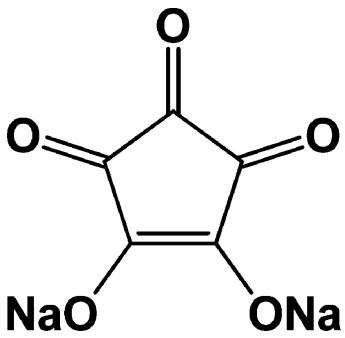

Figure 1.3: Molecular structure of Croconic acid disodium salt

lation of redox potentials, among other things.[22–24]

1.2 Croconic Acid Disodium Salt - Electrode Material

Croconic acid comes from the family of compounds called oxocarbon acids.[17] The oxocarbon acids include deltic, squaric, croconic and rhodizonic acids. These family of compounds are intriguing because of their structural analogy to benzene.[17, 25] In this work we focus on using Croconic acid disodium salt as potential battery material. Sodium salt of croconate dianion or CADS exist as dihydrate in crystal form. CADS has cyclopentene backbone with three carbonyl group and two carbons connected to each other with a double bond as shown in figure 1.3. Crystals of croconic acid derivatives have been known for quite some time as highly conjugated planar structures. CADS was first isolated and studied by Braga et al.[26] The electron density, structure and topography studies of salts of croconic acids have also been extensively carried out to understand the aromaticity and pi conjugation of these materials.[27] The croconate dianion have uniform pi electron distribution with a negative two charge providing a well conjugated network for facile electron diffusion.

Carbonyl compounds have been preferred in literature for electrode materials because of their redox property of readily reducing to their alcohol form and reoxidizing

to their original state. This leads to their higher charging and discharging capabilities when compared to their other organic and inorganic competitors.[28, 29] CADS can theoretically provide a capacity of 288 $Ahkg^{-1}$.[30] In light of all these unique properties, CADS nanowires were synthesized and their properties were explored.[30] The highly conjugated system of CADS can, in principle, provide facile Li ion diffusion. However, CADS when experimentally synthesized as battery material undergoes cracking upon charging.

Along with synthesizing new compounds, computational studies for predicting the structure and properties of these complex compounds is almost a necessity. Mostly current efforts concentrate on synthesis and testing of new sustainable molecules.[31–33] Structural and electronic properties at atomic level play a vital role in understanding the stability of these electrode materials. Understanding the relationship between molecular structure and electrochemical performance not only will aid in synthesizing new materials but will also give a deeper understanding of the working of the battery materials. Only with computational investigations parallel to experimental studies one can hope to pioneer in successfully meeting energy requirements of the fast pacing technical industry. Electrode materials have been reviewed in the past to understand and predict the properties of cathode materials.[11, 13]

We believe that a detailed structural analysis of the battery materials, followed by computationally modelling the ”charging” of the battery can help solve the some of the challenges we face concerning these batteries. We report theoretical insights into the crystal structure and usability of CADS as organic electrode material. Due to the large size of CADS crystals, it is imperative to use computationally efficient methods to study this crystal. In order to achieve an optimum balance between accuracy and

computational cost, a thorough molecular dynamics study has been carried out in this work. Molecular dynamics work on the principle of Newtonian mechanics, details of which are explained in the following section.

1.3 Molecular Mechanics

Molecular mechanics is a method that models atoms and molecules using Newton's laws of motion. The individual treatment of electronic and nuclear motion is a computationally expensive task hence not advisable for large molecular systems. So in classical molecular dynamics, the atoms are treated as one single entity, by ignoring electronic motion and using nuclear motion alone to describe atomic behavior. A convenient way for the same is to follow the Born Oppenheimer (BO) approximation. The BO approximation states that due to a large mass difference between nuclei and electrons, the nuclear and electronic motion can be separated from each other. They can be modeled to move independent of each other.

$$\Psi_{\text{total}} = \psi_{\text{electronic}} \otimes \psi_{\text{nuclear}}$$

The nuclear motion is then governed by classical Newton's laws of motions. The laws of motions are used to define *static* energies and conformations of the systems. Various atomic and molecular properties including bond distances, dihedrals, inter and intra molecular interactions are calculated. The nuclear coordinates are used to construct potential energy surfaces and molecular properties. Since, electron correlation is ignored in this particular approach, the nuclear motion evolves into a single potential energy surface.

The MM method is also known as force field method. Force fields are defined as

collection of parameter sets used to guide molecular motions. The force fields basically express energetics of the system. They are numerically defined and can be customized as per need. That being said, the force field parameters are usually derived jointly for a class of systems such as organic liquids, polymeric systems, biomolecular systems etc. The said parameters defined in force field can be derived by experimental data such as crystal structure, vibrational and /or microwave spectra. Quantum mechanical calculations are also used to derive accurate parameters.

There are a number of force fields which are being used extensively for molecular mechanics calculations. Some of them are CHARMM, AMBER, OPLS, GROMOS among others.[34–37] The testing of these force fields entails conformational calculations with a family of molecules, spectral analysis of the systems and in some cases, potential energy scans using quantum mechanics.

Potential Energy derived from molecular mechanics are used in molecular dynamics simulations of mostly large systems. Dynamics are used to calculate molecular motion over certain time period. The behavior of atoms and molecules, such as bond stretching, surface fluctuation, changes with pressure or temperature variations are observed under certain thermodynamic conditions over a period of time. The forces used to describe this are specified in force field files.

There has been extensive research on optimizing force fields for varied chemical problems. Force fields have been time and again reparameterized in order to suit the requirements of the system in question. Organic liquids, proteins, polyketides, organometallics, organic crystals, among other systems are some of the examples of the class of molecules that were reparameterized before beginning the molecular dynamics studies.[36, 38–42] Bernardes et al studied solid organic crystals with OPLS-AA force

field.[41] Their research suggested a thorough parameterization of the solid ionic crystals claiming that electrostatics and thermodynamic properties of the crystals can vary with the selection of force field parameters. Specially, the evident difference between crystal polymorphs can be seen if the force field is tailored to the need of the system in study.

However, an accurate description of oxocarbon acid crystals has not yet been studied before in the literature. Hence, the tailoring of the OPLS-AA force field was considered as first and one of the most important part of our molecular dynamics studies. The partial charges provided in the original force field, permits only having a neutral system of carbons and oxygen. However, since our crystal had croconate dianion and sodium cations, partial charges needed to be adjusted to maintain charge neutrality.

Following chapter describes the detailed analysis of the Croconic acid disodium salt crystal structure. The calculations were carried out using molecular dynamics. The OPLS-AA force field[36] was reparameterized wherever necessary, and applied to the crystal. The parameters were determined by *ab initio* quantum mechanical calculations on the CADS molecule. The experimental crystal was compared to a newly found crystal phase using thermodynamic free energy calculations. The next chapter is dedicated to analyzing the charging of the CADS crystal with lithium-ion electron pairs. The root mean square deviations are analyzed further to study the stability of the crystal and the behavior of lithium ions within the charged crystal.

Chapter 2

Exploration of CADS Crystal

2.1 Crystal Structure Information

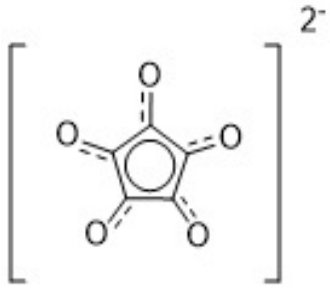

Figure 2.1: Structure of croconate dianion used to study force field parameters

We constructed a crystal with 72 ion pairs of CADS dihydrate. This crystal served as our model electrode for the LIBs. The crystal has monoclinic symmetry with cell dimensions a = 52.098 Å, b = 15.494 Å, c = 19.207Å, α = 111.799°, β = 90.00°and γ = 90.000°. One molecular unit of the crystal has the formula $Na_2C_5O_5.2H_2O$. The CADS and its respective croconate ion with the formula $C_5O_5^{2-}$ is shown in figure 1.3 and 2.1.

Our electrode model was based on experimentally obtained crystal structure as shown in 2.2.[26] The X-ray studies show an interplanar distance of 3.12 Å with C-

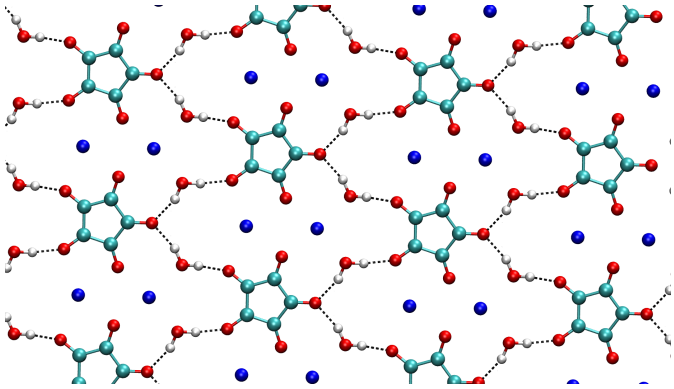

Figure 2.2: XY view of the experimental crystal structure which served as starting structure for all MD calculations, unless otherwise specified.

C distance of 1.248 Å and C-O distance of 1.461 Å in the CADS crystal. The coordination number of the Na^+ ions in the crystal is six, and the oxygen atoms of four croconate dianions and two water molecules occupy the vertices of an octahedron which was maintained for our electrode.

2.2 Molecular Dynamics

We performed the Molecular Dynamics (MD) calculations using TINKER software.[43] TINKER is an easy to use software consisting of wide variety of programs for molecular mechanics and molecular dynamics calculations. Tinker molecular dynamics software uses the coordinates of each atom in the crystal. We used .XYZ file to provide Cartesian coordinates of all the atoms in the crystal. Another important information to be included in the Cartesian file is the atom type according to the force field followed by the connectivity information of each atom.

A force field file with an extension of .PRM is an integral part of any molecular mechanics calculation. The force field used in our work is an All Atom (AA) field - OPLS. The basic structure of force field file consist of atom description, with an assigned

atom type. This is followed by bond stretching information of each atom type, angular parameters description with other atoms and torsional angles for various atom combination. The bonded parameters described above were defined and were customized for the molecular entity needed, in our case CADS. As per classical mechanics, the atoms and molecules are treated as harmonic oscillators. The parameters described were the spring constants along with equilibrium values of bonds, angles and torsions respectively. Bond stretching and angle bending were represented by equations 2.1 and 2.2 in the force field. The spring constants in the aforementioned equations were adjusted by quantum mechanical calculations. With selected k values, potential energy surface was constructed to find equilibrium bond distances and angles. The x coordinate of the minima of these PES were taken as r_{eq} and θ_{eq}. Equation 2.3 described the torsional angles in the force field. ϕ_i here describe dihedral angle, f_i's are phase angles, and V_i represent Fourier coefficients.

$$E_{\text{bond}} = \sum_{bonds} k_r(r - r_{eq})^2 \tag{2.1}$$

$$E_{\text{angle}} = \sum_{angles} k_\theta(\theta - \theta_{eq})^2 \tag{2.2}$$

$$E_{\text{torsion}} = \sum_i \frac{V^i{}_1}{2}[1+\cos(\phi_i + f_i 1)] + \frac{V^i{}_2}{2}[1+\cos(2\phi_i + f_i 2)] + \frac{V^i{}_2}{2}[1+\cos(3\phi_i + f_i 3)] \tag{2.3}$$

Apart from bonded parameters, non bonded interactions were defined in the force field file. For OPLS, Coulomb and Lennard Jones (LJ) potential is used to describe the non bonded interactions. In equation 2.4, the first term represents coulomb interaction and the next two terms represent LJ interaction. the term associated with the power 12

describe the Pauli repulsion forces wheres the term with power 6 is associated to van der Waals attractive forces.

$$E_{\mathrm{ab}} = \sum_{i}^{on\ a} \sum_{j}^{on\ b} [q_{\mathrm{i}} q_{\mathrm{j}} e^2 + 4\epsilon_{\mathrm{ij}} (\sigma_{\mathrm{ij}}{}^{12}/r_{\mathrm{ij}}{}^{12} - \sigma_{\mathrm{ij}}{}^{6}/r_{\mathrm{ij}}{}^{6})] f_{\mathrm{ij}} \tag{2.4}$$

The thermodynamic description along with structural details of our computational model were provided in the key file. Sample of .KEY file used in our calculations is shown in Appendix A.

2.3 Force Field Optimization

2.3.1 Computational Details

Generating force fields for ionic crystals is a challenging undertaking, as the cohesive forces in the crystal involve a delicate balance between electrostatic and the non-bonding interactions.[41] This balance is difficult to find, and no clear prescriptions to achieve it exist to date. Moreover, the charges already present in OPLS force field are not tailored for dianion ring systems (such as croconate). However, considering the nature of molecular entity, $Na_2C_5O_5$, still not described by the existing OPLS force field, a quantum mechanical calculation of partial charges was believed to be most appropriate. The force field also does not hold for molecular dynamics at elevated temperatures for our organic crystal. During long dynamics, the crystal structure has large fluctuations when studied under the original force field.

We performed charge analysis of $Na_2C_5O_5$ at hybrid functional level of theory with the B3LYP method [44, 45] and the TZP Slater-Type orbital basis set[46] with the ADF computer software [47].The results were duplicated with ORCA software[48] at the

MP2 level of theory[49] employing the 6-311G(d) Gaussian type orbital basis set.[50, 51] The partial charges for water molecules were adapted from the TIP3P model for water clusters.[52]

The internal degrees of freedom namely bond stretching and angle bending follow harmonic potentials with a force constant, K in OPLS-AA force field. In order to find equilibrium values of degrees of freedom and spring constant, energy optimization of a single molecule of Croconate dianion ($C_5O_5^{2-}$) was performed with MP2 method and 6-31+G(d,p) in Gaussian16 software.[53] Upon obtaining the equilibrium degrees of freedom from optimized structure, a potential energy scan was performed to derive the force constants from *ab initio* calculations at CCSD level[54] with 6-31+G(d,p) basis set.[50, 51] In this method, the second derivative matrix (the Hessian matrix) from an *ab initio* calculation is used to reproduce the vibrational energies assuming harmonic potentials. The potential energy scan of CCSD method and of OPLS force field was mapped together. The aim of the calculations was to find an agreement between *ab initio* quantum mechanical simulations and MD simulations.The values of spring constant that achieved maximum over of PES for classical and quantum mechanical calculation were chosen. These obtained force constant were then plugged into OPLS-AA force field[36], which guided all the future dynamics.

The constants for dihedral angles for croconate crystal in OPLS force field were in excellent agreement with the PES scan of QM methods. Due to the planar structure of croconate dianion, there was a little need to adjust the torsional bending paramteres and equilibrium values in the force field. The non bonded parameters were also directly adapted from the original OPLS force field. Since they were based on Lennard Jones potential model, both long and short range interactions were covered for atoms in our

crystal.

2.3.2 Results and discussion

Force constants were derived as described above. During charge analysis, specifically CHELPG charges in the MP2 calculations and multipole-derived charges in the DFT calculations were computed. These represent the electrostatic potential more accurately than other population analysis (e.g., Mulliken or Becke).[55] The charge analysis of CADS thus provided the partial charges for the each individual atoms. The partial charges computed from the MP2 calculation are shown in figure 2.3.

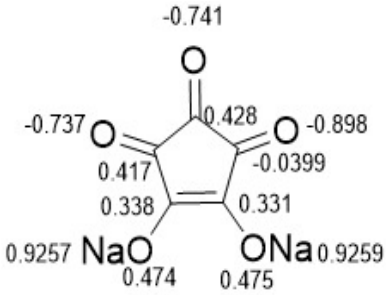

Figure 2.3: Individual partial charges computed for CADS

The individual partial charges were averaged for carbon, oxygen and sodium atoms, to give a single partial charge of each atom. Results are collected in Table 2.1.

Table 2.1: Initial computed atomic charges

Atom	Charges from DFT	Charges from MP2	DFT/MP2 Ratio
C	0.3764	0.2948	1.28
O	-0.8504	-0.6651	1.28
Na^+	1.1851	0.9258	1.28

The actual value of partial charges at hydrid DFT and MP2 are different as shown in

column II and III of table 2.1. However, the ratio of these charges as shown in column IV of Table 2.1 provides us a linear relationship between the partial charges of the two methods. As the further rescaling of these charges also happen in a linear fashion, the difference in the actual number holds very little importance.

Following this, the magnitude of the charges was further adjusted by linearly scaling the charges (multiplying them by a constant) in order to minimize the differences between the physically observed crystal (by X-Ray crystallography [26]) and the theoretical model as shown in figure 2.10a.This was achieved by first translating the charges into our OPLS-AA force field. The charges were further rescaled by analyzing molecular dynamics trajectories until the RMSD of the crystal compared to the original crystal structure was minimum. Partial charges obtained during some stages of rescaling are shown in Table 2.2.

Table 2.2: Initial computed atomic charges

Atom	Stage A	Stage B	Stage C
C	0.2856	0.3067	0.3089
O	-0.6452	-0.6929	-0.6979
Na	0.8990	0.9655	0.9725

Figure 2.4a shows how the charges in Stage A are not appropriate. This is because the RMSD of the Na ions first shows a sort of equilibration (at round t=2ps), but then there is an abrupt change in structure yielding a RMSD = 4 Å. This indicates that the crystal melts with this particular choice of atomic charges.

Figure 2.4b shows how the charges in Stage B are already close to yield a physical picture. This is because the RMSD of the Na ions is capped at RMSD = 0.3 Å. This

indicates that the crystal remains solid with this particular choice of atomic charges at room temperature.

Figure 3 shows how the charges in Stage C are only slightly better than the ones in Stage B. The RMSD of the Na ions is capped at RMSD = 0.28 Å. This indicates that the crystal remains solid with this particular choice of atomic charges at room temperature. Despite further optimization, we could not improve upon the charges obtained in stage C. Thus, we chose these charges as final and employ them in any subsequent simulation.

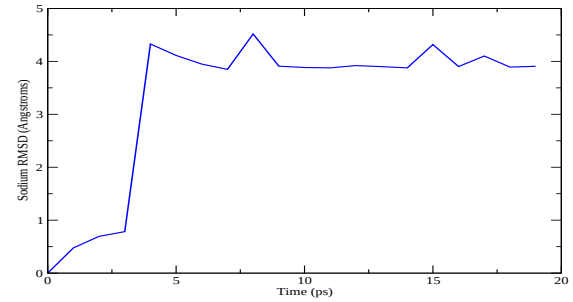

(a) RMSD of Na ions in sodium croconate obtained with atomic charges in STAGE A.

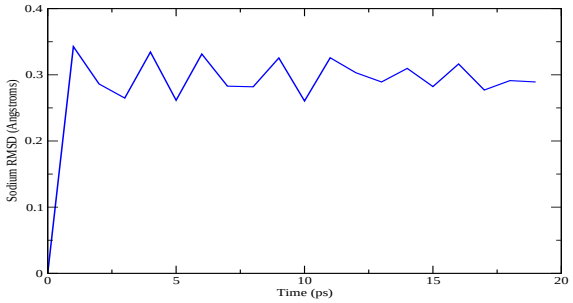

(b) RMSD of Na ions in sodium croconate obtained with atomic charges in STAGE B.

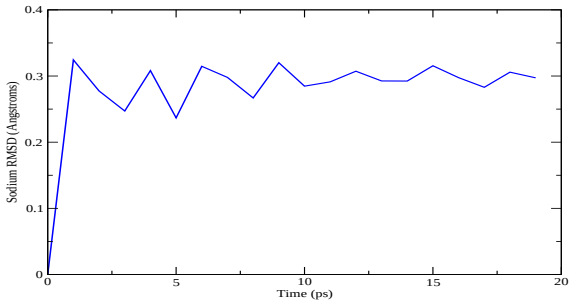

(c) RMSD of Na ions in sodium croconate obtained with atomic charges in STAGE C.

Figure 2.4: RMSD of Na ions calculated for each stages given in Table 2.2.

The Van der Waals interactions were described by Lennard-Jones potential characterized by an atomic diameter, σ and an interaction parameter ε. the σ and ε parameters were extracted as it is from the original OPLS-AA force field.

The plots in figures 2.5, 2.6 and 2.7 show the potential energy surface scans for bond stretching, angle bending and torsional bending parameters with the mentioned force

constants in table 2.3. The magnitude of the curve representing ΔE remains minimal for figures 2.5 and 2.7 indicating that the force field with adjusted parameters work well for a single croconate dianion. For figure 2.6, the angle stretching beyond the minima leads to a very high ΔE, which is understandable as the degree of freedom includes alterations in carbon - carbon bond length as well. This results in a cumulative degree of freedom, which is not only dependent on CCC angle but CC bond as well.

Tables 2.3 and 2.4 lists the final values of altered bond and angle force constants, along with altered atomic partial charges, and Van der Waals interaction parameters. The resulting force field is used to guide MD calculations for the complete crystal under periodic boundary conditions (refer appendix B).

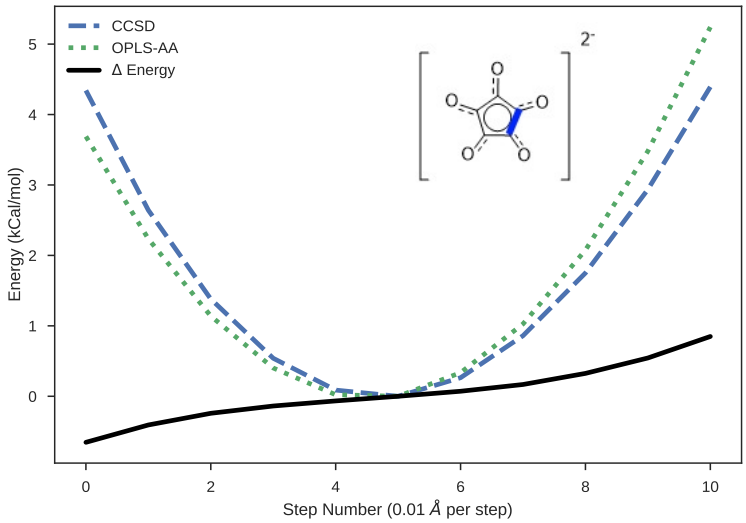

(a) Potential energy scan of the CC bond relaxation as a function of bond stretching (in Å). All the CC bonds, (one of which is highlighted in blue in croconate dianion structure) were relaxed and contracted to get a potential energy scan around the minimum. At every step in the plot, the bond was contracted/ stretched by 0.01Åcentered around the optimized bond length.

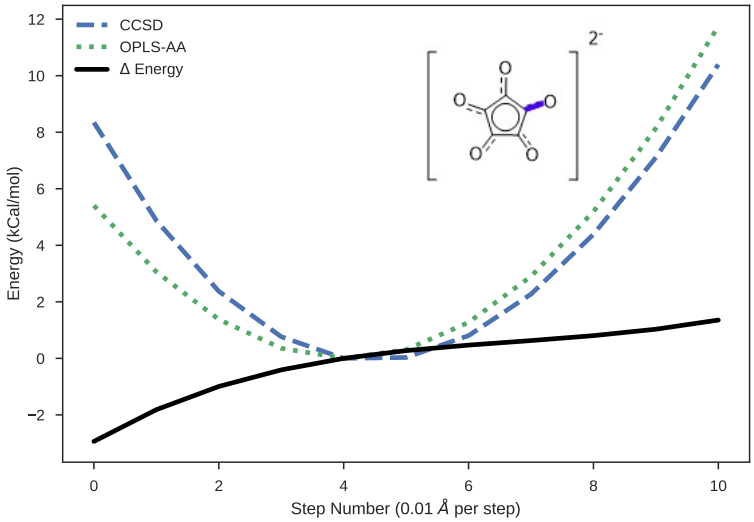

(b) Potential energy scan of the CO bond relaxation as a function of bond stretching (in Å). All the CO bonds, (one of which is highlighted in blue in croconate dianion structure) were relaxed and contracted to get a potential energy scan around the minimum. At every step in the plot, the bond was contracted/ stretched by 0.01Åcentered around the optimized bond length.

Figure 2.5: Bond parameter optimization for the force field

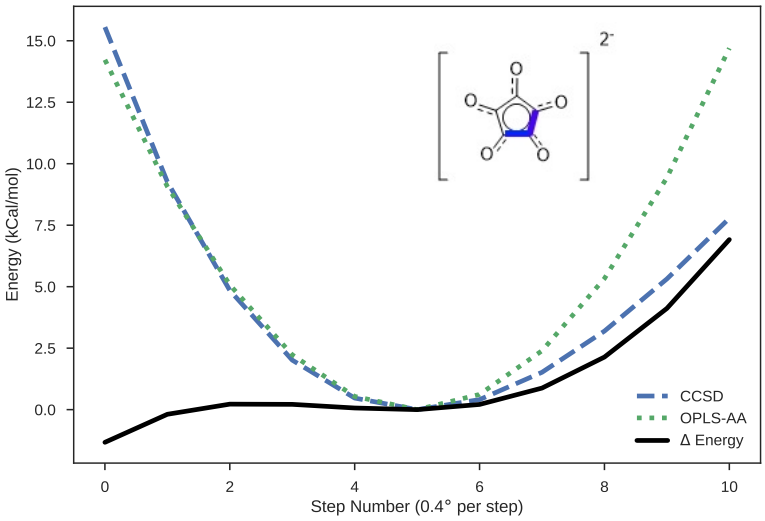

(a) Potential energy scan of the CCC angle relaxation as a function of angle bending. All the CCC angles, (one of which is highlighted in blue in croconate dianion structure) were increased and decreased to get a potential energy scan around the minimum. At every step in the plot, the angle was increased/decreased by 0.4° centered around the optimized bond angle.

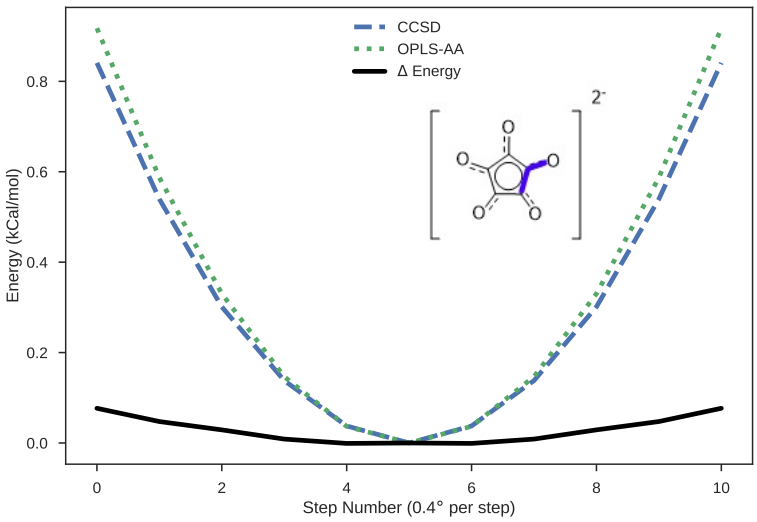

(b) Potential energy scan of the CCO angle relaxation as a function of angle bending. All the CCO angles, (one of which is highlighted in blue in croconate dianion structure) were increased and decreased to get a potential energy scan around the minimum. At every step in the plot, the angle was increased/decreased by 0.4° centered around the optimized bond angle.

Figure 2.6: Angle parameter optimization for the force field

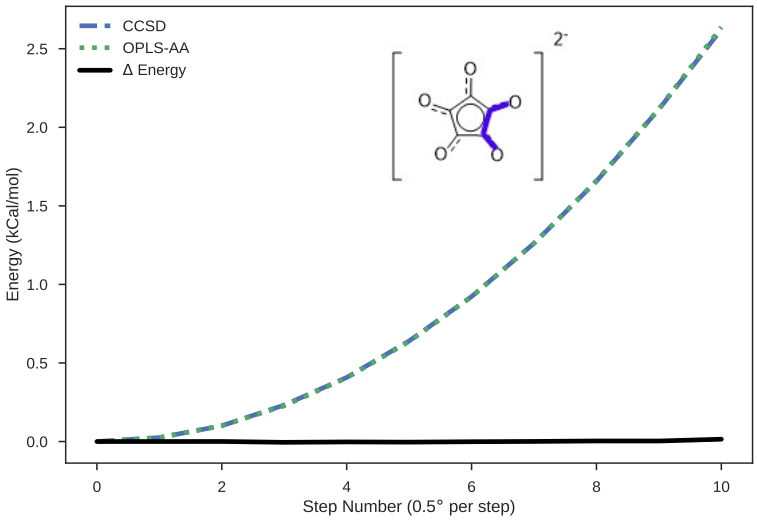

Figure 2.7: Potential energy scan of OCCO dihedral angle relaxation as a function of dihedral angle bending. All the OCCO dihedral angles, (one of which is highlighted in blue in croconate dianion structure) were increased to get a potential energy scan starting from the minimum. At every step in the plot, the angle was increased by 0.5° from optimized dihedral angle value of 0°

Table 2.3: Bond stretching and angle bending force constants. Values in the brackets show the original OPLS-AA parameters. The original parameters for Oxygen(OW) and Hydrogen(HW) for water molecules are original TIP-3P parameters[52] present in the OPLS-AA file

Bond	K (kcal/mol/Å^2)	Angle	K (kcal/mol/rad^2)
C-C	3000(350)	C-C-C	250 (63)
C-O	2600(570)	C-C-O	65(80)
OW-HW	600	HW-OW-HW	75

Table 2.4: Intermolecular Interaction Parameters used in the OPLS-AA force field. The brackets in column 2 show original partial charges present in the OPLS-AA force field.

Atom	Charge	σ(Å)	ε(kcal/mol)
C	+0.3089(0.4700)	3.75	0.1050
O	-0.6979(-0.4700)	2.96	0.2100
OW	-0.8340	3.15	0.1521
HW	+0.4170	0.00	0.0000
Na	+0.9725(1.000)	4.07	0.0005

2.4 Selection of τ-Pressure for barostat

The MD simulations take place under certain thermodynamic conditions, for the system to be able to replicate experimental conditions. A check on the state variables of the system ensures close to real-life experimental conditions. There can be different thermodynamical ensembles to control state variables such as Canonical ensemble (NVT), Microcanonical ensemble (NVE) and Isobaric-Isothermal ensemble (NPT). In our work, the crystal was equilibrated in NVT and NPT ensembles. Both these ensembles maintain a thermal equilibrium with heat bath which is of paramount importance while studying the effects of temperature on crystal stability. Moreover, these two ensembles closely resemble experimental conditions of studying battery materials. TINKER software uses thermostat and barostat developed by Berendsen et al to control pressure and temperature of the system.[56] The main purpose of a barostat is to change instantaneous pressure tensor so that the external pressure remains constant.[57] The Berendsen barostat adds an extra term to the Langevin equations of motion which

has an effect on the dynamics of the system. An important parameter of this effect is the barostat relaxation time τ. The relaxation time is the measured timescale of system's reaction to external pressure. A very low τ, indicates a strong interference to the motion of the particles within the system. On the contrary, a high τ affects the system's fluctuations a bit more slowly.

2.4.1 Computational Details

The Berendsen thermostat/barostat in TINKER use a default relaxation time(τ) of 0.1ps/2.0ps respectively to maintain the required ensemble condition. However, the MD calculations with pressure τ = 2.0 ps, gave fluctuations in instantaneous pressure in the range of 1000 atm. In order to decrease these instantaneous pressure fluctuations, we performed a series of 100 ps test MD simulations at T = 298K and average P = 1 atm at different τ values. The aim was to find the best compromise between the relaxation time and the accuracy of dynamic runs. Simulations were run under NPT ensemble conditions with τ of the thermostat being constant at 0.1ps. The instantaneous pressure, volume and temperature was recorded every 0.1 ps (or 100 fs) and a snapshot of the dynamics was recorded every 0.5 ps.

2.4.2 Results and Discussion

Under NPT ensemble conditions, maintaining a constant pressure is usually a tedious task. We selected pressure τ of 0.2, 0.5, 1.0 and 2 ps. For each pressure τ, MD runs were performed as described in computational details. The recorded instantaneous pressure was averaged over the complete dynamic run for each τ. We believed that τ=1.0 ps had the best balance between dynamics and pressure fluctuations. At 1.0 ps, the resultant

average pressure was reduced to 1.4 atm in comparison to 1.8 atm at τ=2.0 ps while maintaining an accurate physical picture.

Figure 2.8 shows that the relationship between relaxation time and pressure is not linear. This is understandable as lower the τ value, the more the barostat's interference with dynamics of the system. As a best compromise, τ = 1.0 ps was selected for further dynamic runs. As we proceeded with carrying out 1 ns simulations at later stages, the average pressure of the runs improved by a more considerable amount proving that τ of 1.0 ps was indeed the right choice.

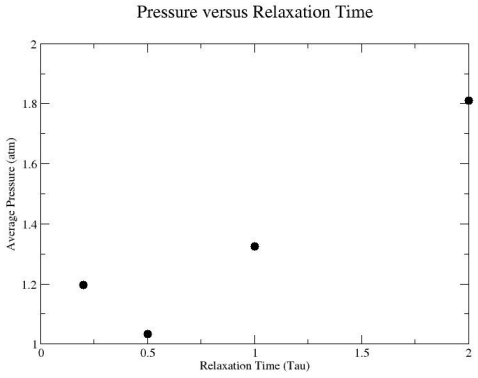

Figure 2.8: Average Pressure (in atm) versus the relaxation time (τ) of Berendsen barostat.

2.5 Heating of CADS Crystal

A MD run works when the system is subjected to the force field for a certain amount of time. The system's energetics were recorded from time to time and these snapshots of the system were analyzed to study the behavior of the molecular system. In our work, we ran each simulation for the total of 1 nanosecond with a time step of 1 femtosecond. That is, the crystal was studied under our force field and the coordinates as well as the velocities were updated every 1 fs. The instantaneous pressure, volume and temperature

was recorded every 0.1 ps (or 100 fs) and a snapshot of the dynamics was recorded every 0.5 ps. The data obtained was divided into equilibration runs and production runs. The system takes a certain amount of time to adjust to the provided dynamic conditions. We therefore let the system equilibrate for the first 750 ps. The remaining 250 ps data were plotted and analyzed as production run.

2.5.1 Effects over Volume of the Battery

Studying the volume increase of the crystal with temperature elevation gives a description of the structural changes that might occur while heating of the battery. The dynamic simulations were first performed at room temperature. The .DYN file of the room temperature runs was used to restart the calculation at 320K, hence maintaining a continuity in the dynamics. The simulations have been performed under constant pressure (1 atm) and the volume of the material can be followed as a function of temperature. A sequential decrease in density is observed with temperature up until 420K, followed by an increase in the density when the system was heated to 470K. This density increase is because of phase transition to phase 2. The observed denser polymorph was cooled from 470K to room temperature. Phase 2 was stable at room temperature. The phase diagram is shown in figure 2.9. At room temperature, there is a decrease of 3.3 $\%$ in the volume as the crystal shrinks from phase 1 to phase 2.

2.5.2 Thermodynamic Analysis of Crystal Structure

The interplanar distance does not significantly change upon heating. The presence of another phase, was observed upon heating of the crystal. This new phase has been previously unknown and thus named arbitrarily as phase 2. The interplanar distance along

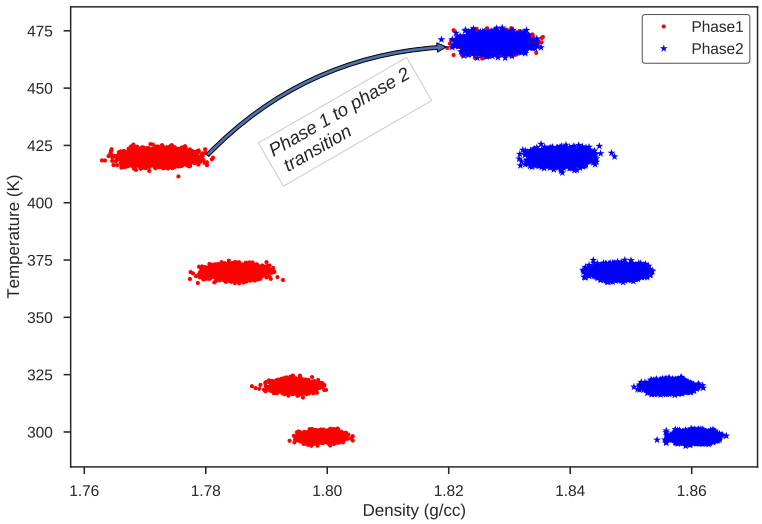

Figure 2.9: Temperature as a function of Density (g/cc). The crystal is shown to have a significantly higher density after 420K which is attributed to an altogether different phase of the crystal (henceforth called as phase 2). The crystal at 470K is cooled to room temperature, is shown by the red curve in the plot.

z direction was similar for both the crystal structures. The crystal viewed down from z axis is shown in figure 2.10. The structures show significant differences in the relative arrangement of croconate dianions and sodium atoms. The resultant configuration of phase 2, when compared to experimental crystal phase, has croconate dianion alignment in a straight line which changes the hydrogen bonding network significantly, shown by dotted lines in figure 2.10. The symmetrical H-bonding network of the crystal phase now changed to layered H bonding.

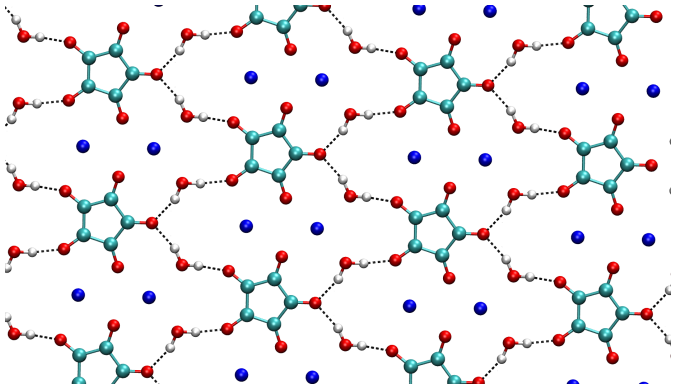

(a) XY view of the experimental crystal structure which served as starting structure for all MD calculations, unless otherwise specified. The visualization of the crystal in figure was done in VMD software.[58]

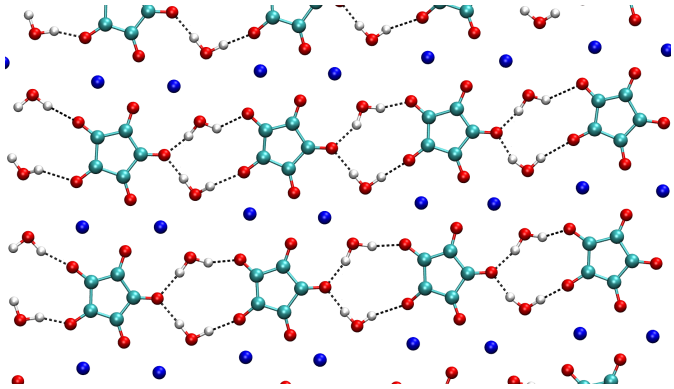

(b) XY view of phase 2 of the crystal obtained about heating of the crystal.

Figure 2.10: The structure of Croconic Acid Disodium Dihydrate as viewed down from the z-axis. The visualization of the crystal in figure was done in VMD software.

The crystal as viewed down from y axis is shown in figure 2.11. The rings in the experimental structure do not overlap in each layer. A shift of about 3 Å is observed between the ring centroids. This shifting of the centroids do not change significantly in the new phase 2. The stacking of the croconate rings exhibit similar behavior in phase 2.

The apparent bending of the crystal structure in figure 2.11b is a reaction to thermodynamic constraints. The structure of phase 2 under pressure constraints of the barostat exhibit rippling, a phenomena commonly observed in 2D graphene sheets.[59] Each layer of the crystal is not perfectly flat but undergoes some bending with thermal fluctu-

ations under constant pressure. The slight elevation in layers of phase 2 of the croconate crystal as shown in figure 2.11b is therefore not a mark of instability but an effect of thermodynamic conditions imposed on the system.

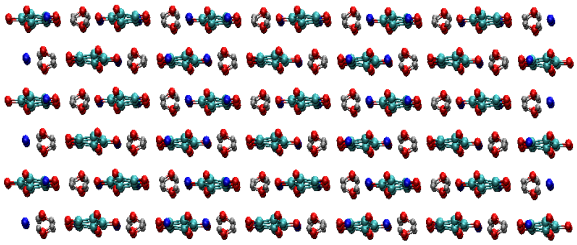

(a) XZ view of the experimental crystal structure which served as starting structure for all MD calculations. The structure shows shift between ring centroids in each layer. The croconate rings do not superimpose each other perfectly.

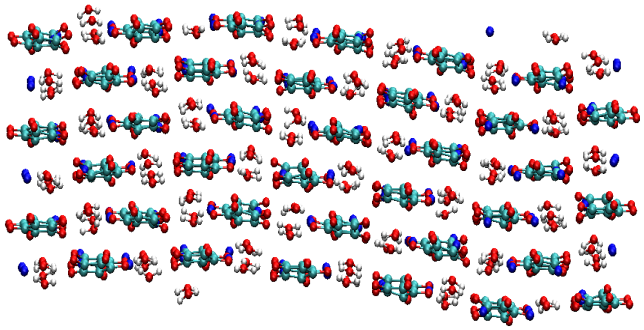

(b) XY view of phase 2 of the crystal obtained about heating of the crystal.

Figure 2.11: The structure of Croconic Acid Disodium Dihydrate as viewed down from the y-axis. The bent shape of the crystal in figure 2.11b is due to a phenomenon called rippling.

The stability of the two structures was studied by calculating the Helmholtz free energy of the two crystal phases. The partition function and consequently the free energy was plotted with increasing temperature. The data was sampled from the production run of NVT ensemble. Free energy, given by equation 2.6 was calculated with the following formulas :

$$Q = \sum_{i=1}^{n} \exp^{-\beta E_{\mathrm{i}}} g_{\mathrm{i}} \Delta E \tag{2.5}$$

$$A = -\frac{1}{\beta} \log Q \tag{2.6}$$

where, $\beta = \frac{1}{kT}$ and $\Delta E = E_{\text{i}} - E_{\text{i-1}}$. Q in equation 2.5 is the partition function calculated at each temperature, n is the number of energy bins the system is divided into (in our case n=10) and g_i is the occupation number of each bin with the corresponding energy E_i.

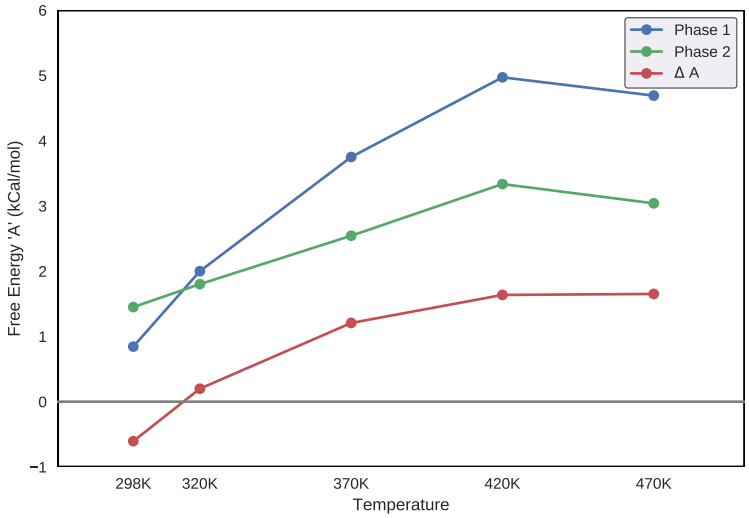

Figure 2.12: Free energy (in Kcal/mol) versus the temperature of the crystal. The blue curve here shows the free energy of the crystal in phase 1 and the green curve shows the free energy of the crystal in phase 2. Curve in red is the free energy difference between phase 1 and phase 2.

From figure 2.12, we can see that the crystal is more stable in the phase 1 at room temperature and then as the temperature increases, the free energy of phase 2 is lower than phase 1. The RMSD plot of the crystal in chapter 4 indicate random high energy motions after 370 K , which results in some errors in free energy calculations, as seen in the divergence of blue and green curves.

Chapter 3

Charging of the CADS Crystal with Lithium

A computational model was fashioned with the purpose of mimicking charging of the electrode material. Lithiation of an electrode is defined as addition of lithium ion into the electrode. We performed lithiation in two steps. Firstly a lithium ion-electron pair was added to the crystal model. No bbond making or breaking were involved in the charging. The idea was to observe the behavior of electrode material in the presence of a lithium ion. The electron was arbitrarily added to one croconate dianion hereby reducing it to croconate trianion.

$$C_5O_5^{2-} + e^- \rightarrow C_5O_5^{3-} \tag{3.1}$$

There is not any definite mechanism of lithium insertion into the electrode. Therefore, we modeled our lithiated crystal in such a way that a lithium ion was added between two layers of the croconate sheets. In order to maintain charge neutrality and for sustainable electrostatics of the system, an electron was added to a croconate ion, as described in above equation. Therefore, leading to a redox reaction, where the crystal on one hand

is oxidized by the presence of lithium ion,and an arbitrary croconate dianion is reduced by an extra electron.

The second step was to add another lithium electron pair to the above charged crystal. The crystal in this step had one CADS with a negative four charge and two lithium ions placed at arbitrary locations within the crystal structure.

$$C_5O_5^{3-} + e^- \rightarrow C_5O_5^{4-} \tag{3.2}$$

3.1 Computational Details

The partial charges of the croconate anions in the lithiated crystal were also obtained at MP2 level of theory using 6-311G(d) basis set. The lithiated crystal structures were minimized at room temperature in TINKER software. The MD simulations of this charging event were step wise performed at 298K followed by 320K, 370K, 420K and 470K. The key file as shown in appendix A guided all the MD simulations. As before, the total simulation time as 1 ns, where the first 75% of it was equilibration run and the last 25% was recorded as the production run. The force field parameters were also used as specified in appendix B.

3.2 Results and Discussion

The resultant charge and other non bonded interactions for triply and quadruply charged croconate anion are given in table 3.1.

Table 3.1: * and ** refer to triply and quadruply charged croconate molecule upon adding one and two Lithium-electron pair respectively.

Atom	Charge	σ(Å)	ε(kcal/mol)
C*	+0.2659	3.75	0.1050
O*	-0.8549	2.96	0.2100
C**	+0.4109	3.75	0.1050
O**	-1.1999	2.96	0.2100

Interestingly, the lithiated crystal structure, when minimized with respect to the nuclear coordinates, settles on the energy minima of the phase 2. That is, upon lithiation the system chooses phase 2 at room temperature. This leads to the volume shrinking by 2.8 $\%$ upon charging, as the crystal transitions from phase 1 to phase 2. These phase non uniformities have been known to occur during Li ion insertion in solid electrodes, causing mechanical strain in the electrodes.[60] Experimental results of CADS charging indicate presence of cracks in the electrode upon charging.[30] We believed that the preference of the crystal towards a more dense phase 2 crystal would have caused the development of cracks in the battery upon charging.

After minimizing the lithiated crystal, MD calculations were carried out upon sequential heating of the crystal. The percentage change in volume upon lithiation was plotted as a function of temperature. Note that since the lithiated crystal prefers phase 2, the base line of the graph in figure 3.1 is the average volume of the phase 2 of the unlithiated crystal. Figure 3.1 shows a increase in crystal volume upon charging. Lithiation of the crystal at room temperature leads to a 0.745 $\%$ increase in volume with each additional 1 $\%$ lithiation.

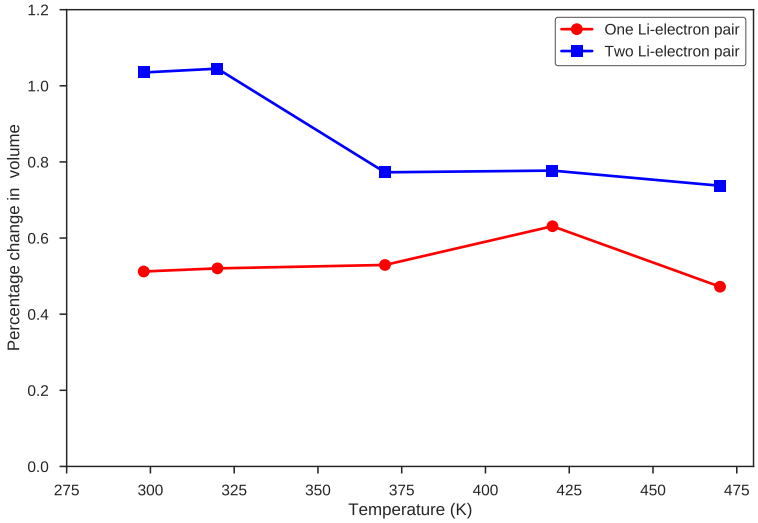

Figure 3.1: Percentage of volume change of the CADS dihydrate crystal upon sequential insertion of one and two lithium ions

Chapter 4

RMSD Analysis

The crystal structure stability, as well as the steadiness of the lithiated crystal was determined by computing root mean square deviations(RMSD) of our MD runs. The root mean square deviations were recorded in VMD. The reference structures for RMSD calculations was first frame of the production run of each crystal. RMSD is calculated by taking each x, y z coordinate for every atom at every time step the snapshot was recorded. This position value is subtracted from the coordinates of the reference structure. The resultant change in coordinate is squared and added together for all the three dimensions. The square root of this added deviation is termed as RMSD, as given in equation 4.1.

$$RMSD(v,w) = \sqrt{\frac{1}{n}\sum_{i=1}^{n}((v_{\text{ix}} - w_{\text{ix}})^2 + (v_{\text{iy}} - w_{\text{iy}})^2 + (v_{\text{iz}} - w_{\text{iz}})^2)} \tag{4.1}$$

Figure 4.1, 4.2a and 4.2b indicate phase transition for unlithiated crystal, beginning around 320 K. The simulations started with experimental crystal structure phase with RMSD of about 0.5Å. The RMSD underwent a significant change of about 4Å at 320K followed by an increase of 2Å at 420K. Due to the absence of the role of the barostat, NVT dynamics showed a more discrete step wise phase change, arriving at similar re-

sults as NPT by 470K. The visualization of structures in the NVT framework, confirmed the crystal structure as shown in figure 2.10. The stability of the crystal upon charging was indicated by the lower values of RMSD for the lithiated crystal. The crystal remained stable with increasing temperature. No melting was observed until 470K.

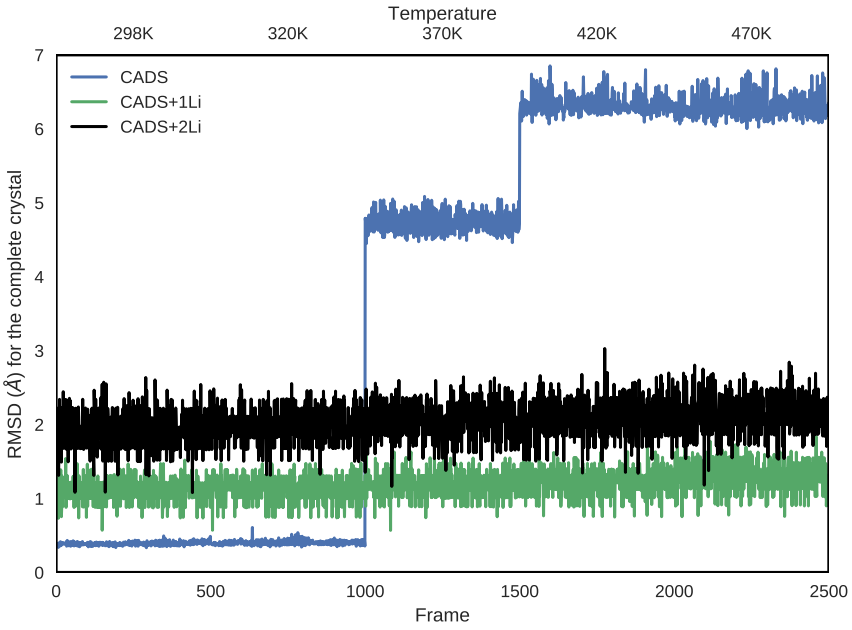

Figure 4.1: RMSD(Å) for the complete crystal

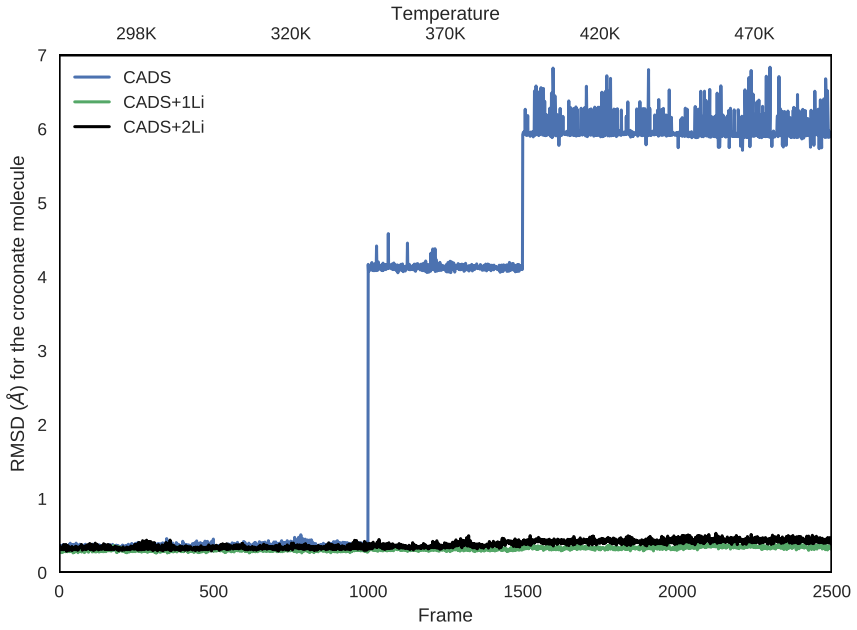

(a) RMSD(Å) for the croconate molecule

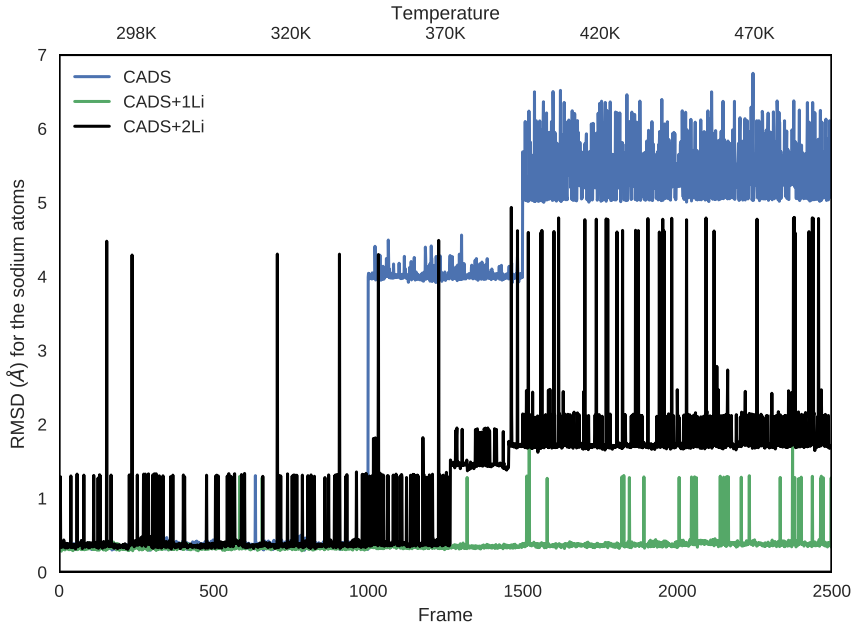

(b) RMSD(Å) for the sodium atoms

Figure 4.2: The plots above contain Root Mean square deviations for unlithiated crystal, after addition of one Li followed by addition of two Lithium. The increase in RMSD to about 6-7 Å for unlithiated crystal shows presence of another crystal structure altogether, hence corroborating our NPT studies in section 2.5.1

The time scale of the simulation was low to detect any significant lithium diffusion, as those require MD calculations on the scale of micro and milli seconds. Nano second simulations are generally not capable of detecting any real atomic diffusion.[13]

The croconate carbons in the vicinity of the lithium ions were isolated. The RMSD of these neighbouring croconates with respect to the uncharged crystal is shown in figure 4.3a and 4.3b. Low values of RMSDs in the vicinity of lithium atom indicate no significant change in the structure of the crystal upon lithiation. This proved that the crystal is stable upon charging with lithium ions.

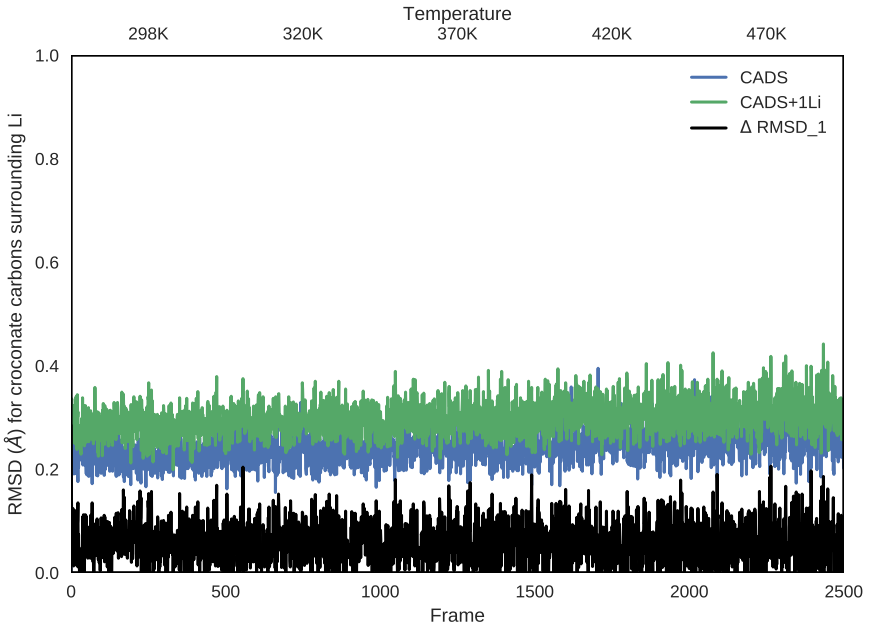

(a) RMSD(Å) for the crystal for carbon atoms of the croconate molecules in the vicinity of Li atom for the crystal charged with one lithium electron pair.

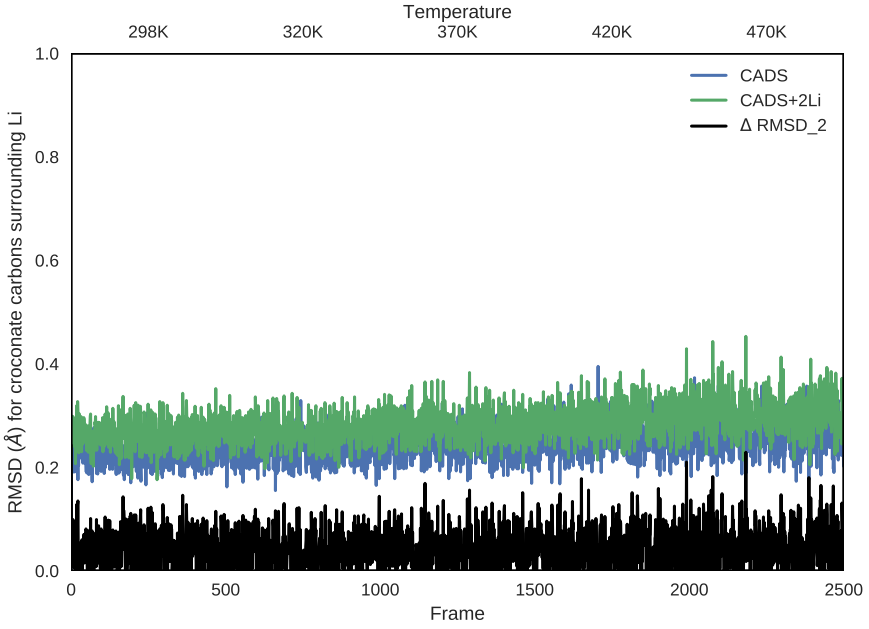

(b) RMSD(Å) for carbon atoms of the croconate dianion in the vicinity of Li atom for the crystal charged with two lithium electron pairs.

Figure 4.3: The plots above contain Root Mean square deviations for the carbons surrounding the added lithium cation. The curves show respectively the RMSDs of unlithiated and charged crystal. The third curve near zero indicate the difference between the two RMSDs

Chapter 5

Conclusion

The OPLS-AA force field was successfully reparameterized for our Croconic acid disodium salt crystal. The resultant force field have been provided in appendix B. MD simulations have been performed on croconic acid disodium dihydrate crystal. The simulations show a presence of a crystal structure, significantly different from the experimental crystal structure. The crystal prefers this new structure upon charging with lithium-ion electron pairs. The phase transition at very early stages of lithium insertion into the CADS crystal is possibly the reason for cracking of the CADS in experimental studies.[30] The volume of the crystal decreases by 2.8 $\%$ upon charging with lithium which explains the short battery cycle lifetime of the CADS dihydrate crystal as electrode material. The thermodynamic analysis was also performed in this work to ascertain the presence of phase 2. Computational results point to a possible new phase of the CADS crystal.

The low values of RMSD with minimal fluctuations show stability of the second phase. Thermodynamical studies corroborate the stability of second phase at room temperature. It is clearly seen from our results that CADS, albeit different in structure

from experimental crystal can withstand the charging and discharging even at elevated temperatures of 470K. However, this is only a starting point and with further experimental studies, the presence or lack thereof of a new crsyal phase can be made certain. If experimentally established, we would propose to assemble batteries for the newly found denser polymorph or at elevated temperatures.

Appendix A

Sample of a .Key file

```
# Output Control

ARCHIVE

VERBOSE

   # Force Field Selection

PARAMETERS oplsaa.prm

   # Ewald Summation

EWALD

   # Crystal Lattice And Periodic Boundary

A-AXIS 52.089

B-AXIS 15.494

C-AXIS 19.207

ALPHA 111.799

BETA 90.0

GAMMA 90.0

   # Dynamics
```

```
TEMPERATURE 298

TAU-TEMPERATURE 0.1

THERMOSTAT BERENDSEN

   #GRADIENT

INTEGRATOR VERLET
```

Appendix B

Customized OPLS-AA force field

atom	1	3	C	”Ketone C=O”	6	12.011	3
atom	2	4	O	”Ketone C=O”	8	15.999	1
atom	5	3	C	”Ketone C=O”	6	12.011	3
atom	6	4	O	”Ketone C=O”	8	15.999	1
atom	222	3	C	”Ketone C=O”	6	12.011	3
atom	223	4	O	”Ketone C=O”	8	15.999	1
atom	63	31	OW	”TIP3P Water O”	8	15.999	2
atom	64	32	HW	”TIP3P Water H”	1	1.008	1
atom	349	69	Na	”Sodium Ion Na+”	11	22.990	0
atom	348	68	Li	”Lithium Ion Li+”	3	6.941	0

```
vdw     63     3.15061    0.1521

vdw     64      0.0000     0.0000

vdw    222     3.7500     0.1050

vdw    223     2.9600     0.2100

vdw    349     4.0700     0.0005

vdw      1     3.7500     0.1050

vdw      2     2.9600     0.2100

vdw      5     3.7500     0.1050

vdw      6     2.9600     0.2100

vdw    348     2.8700     0.0005


bond     3      3    350.00 1.4676

bond     3      4    650.00 1.2452

bond    31     32    600.00 0.9572


angle    3     3     3    250.00    108.00

angle    3     3     4     65.00    126.00

angle   32    31    32     75.00    104.52


torsion   4   3   3   4   1.600   0.0   1   3.200   180.0   2   0.000   0.0   3

torsion   4   3   3   3   1.600   0.0   1   6.200   180.0   2   0.000   0.0   3

torsion   3   3   3   3   1.600   0.0   1   3.200   180.0   2   0.000   0.0   3
```

charge	63	-0.8340
charge	64	0.4170
charge	222	0.3089
charge	223	-0.6979
charge	349	0.9725
charge	1	0.2659
charge	2	-0.8549
charge	348	0.9725
charge	5	0.4109
charge	6	-1.1999

Acronyms

CADS Croconic acid disodium salt. ii, iv, 5, 6, 9–12, 15, 25, 31–34, 40

LIBs Lithium Ion Batteries. 2–4, 10

NPT Isothermal-Isobaric. ii, 23, 24, 36, 37

NVT Canonical Ensemble. ii, 23, 29, 35, 36

Bibliography

(1) Eberle, D. U.; von Helmolt, D. R. *Energy & Environmental Science* **2010**, *3*, 689.

(2) Scrosati, B.; Hassoun, J.; Sun, Y.-K. *Energy & Environmental Science* **2011**, *4*, 3287.

(3) Goodenough, J. B.; Kim, Y. *Chemistry of Materials* **2010**, *22*, 587–603.

(4) Shabani, B.; Biju, M. *Energies* **2015**, *8*, 10153–10177.

(5) Singh, N.; Arthur, T. S.; Ling, C.; Matsui, M.; Mizuno, F. *Chem. Commun.* **2013**, *49*, 149–151.

(6) Hayashi, M.; Arai, H.; Ohtsuka, H.; Sakurai, Y. *Journal of Power Sources* **2003**, *119-121*, 617–620.

(7) Aurbach, D.; Lu, Z.; Schechter, A.; Gofer, Y.; Gizbar, H.; Turgeman, R.; Cohen, Y.; Moshkovich, M.; Levi, E. *Nature* **2000**, *407*, 724–727.

(8) Slater, M. D.; Kim, D.; Lee, E.; Johnson, C. S. *Advanced Functional Materials* **2012**, *23*, 947–958.

(9) Tarascon, J.-M.; Armand, M. *Nature* **2001**, *414*, 359–367.

(10) Bhatt, M. D.; O'Dwyer, C. *Physical Chemistry Chemical Physics* **2015**, *17*, 4799–4844.

(11) Islam, M. S.; Fisher, C. A. J. *Chem. Soc. Rev.* **2014**, *43*, 185–204.

(12) Liu, C.; Neale, Z. G.; Cao, G. *Materials Today* **2016**, *19*, 109–123.

(13) Chakraborty, S.; Banerjee, A.; Watcharatharapong, T.; Araujo, R. B.; Ahuja, R. *Journal of Physics: Condensed Matter* **2018**, *30*, 283003.

(14) Ke, F.-S.; Wu, Y.-S.; Deng, H. *Journal of Solid State Chemistry* **2015**, *223*, 109–121.

(15) Li, C.; Yin, C.; Gu, L.; Dinnebier, R. E.; Mu, X.; van Aken, P. A.; Maier, J. *Journal of the American Chemical Society* **2013**, *135*, 11425–11428.

(16) Han, X.; Chang, C.; Yuan, L.; Sun, T.; Sun, J. *Advanced Materials* **2007**, *19*, 1616–1621.

(17) Song, Z.; Zhan, H.; Zhou, Y. *Angewandte Chemie International Edition* **2010**, *49*, 8444–8448.

(18) Genorio, B.; Pirnat, K.; Cerc-Korosec, R.; Dominko, R.; Gaberscek, M. *Angewandte Chemie International Edition* **2010**, *49*, 7222–7224.

(19) Morita, Y.; Nishida, S.; Murata, T.; Moriguchi, M.; Ueda, A.; Satoh, M.; Arifuku, K.; Sato, K.; Takui, T. *Nature Materials* **2011**, *10*, 947–951.

(20) Chen, H.; Armand, M.; Courty, M.; Jiang, M.; Grey, C. P.; Dolhem, F.; Tarascon, J.-M.; Poizot, P. *Journal of the American Chemical Society* **2009**, *131*, 8984–8988.

(21) Muench, S.; Wild, A.; Friebe, C.; Häupler, B.; Janoschka, T.; Schubert, U. S. *Chemical Reviews* **2016**, *116*, 9438–9484.

(22) Wu, H.; Shevlin, S. A.; Meng, Q.; Guo, W.; Meng, Y.; Lu, K.; Wei, Z.; Guo, Z. *Advanced Materials* **2014**, *26*, 3338–3343.

(23) Araujo, R. B.; Banerjee, A.; Panigrahi, P.; Yang, L.; Sjödin, M.; Strømme, M.; Araujo, C. M.; Ahuja, R. *Physical Chemistry Chemical Physics* **2017**, *19*, 3307–3314.

(24) Janoschka, T.; Hager, M. D.; Schubert, U. S. *Advanced Materials* **2012**, *24*, 6397–6409.

(25) West, R. *Israel Journal of Chemistry* **1980**, *20*, 300–307.

(26) Braga, D.; Maini, L.; Grepioni, F. *Chemistry – A European Journal* **2002**, *8*, 1804–1812.

(27) Ranganathan, A.; Kulkarni, G. U. *The Journal of Physical Chemistry A* **2002**, *106*, 7813–7819.

(28) Wu, X.; Jin, S.; Zhang, Z.; Jiang, L.; Mu, L.; Hu, Y.-S.; Li, H.; Chen, X.; Armand, M.; Chen, L.; Huang, X. *Science Advances* **2015**, *1*, e1500330.

(29) Xu, Y.; Zhou, M.; Lei, Y. *Materials Today* **2018**, *21*, 60–78.

(30) Luo, C.; Huang, R.; Kevorkyants, R.; Pavanello, M.; He, H.; Wang, C. *Nano Letters* **2014**, *14*, 1596–1602.

(31) Guo, W.; Yin, Y.-X.; Xin, S.; Guo, Y.-G.; Wan, L.-J. *Energy Environ. Sci.* **2012**, *5*, 5221–5225.

(32) Han, X.; Qing, G.; Sun, J.; Sun, T. *Angewandte Chemie International Edition* **2012**, *51*, 5147–5151.

(33) Walker, W.; Grugeon, S.; Mentre, O.; Laruelle, S.; Tarascon, J.-M.; Wudl, F. *Journal of the American Chemical Society* **2010**, *132*, 6517–6523.

(34) Weiner, S. J.; Kollman, P. A.; Case, D. A.; Singh, U. C.; Ghio, C.; Alagona, G.; Profeta, S.; Weiner, P. *Journal of the American Chemical Society* **1984**, *106*, 765–784.

(35) Cornell, W. D.; Cieplak, P.; Bayly, C. I.; Gould, I. R.; Merz, K. M.; Ferguson, D. M.; Spellmeyer, D. C.; Fox, T.; Caldwell, J. W.; Kollman, P. A. *Journal of the American Chemical Society* **1995**, *117*, 5179–5197.

(36) Jorgensen, W. L.; Maxwell, D. S.; Tirado-Rives, J. *Journal of the American Chemical Society* **1996**, *118*, 11225–11236.

(37) Mayo, S. L.; Olafson, B. D.; Goddard, W. A. *The Journal of Physical Chemistry* **1990**, *94*, 8897–8909.

(38) Robertson, M. J.; Tirado-Rives, J.; Jorgensen, W. L. *Journal of Chemical Theory and Computation* **2015**, *11*, 3499–3509.

(39) Kahn, K.; Bruice, T. C. *Journal of Computational Chemistry* **2002**, *23*, 977–996.

(40) Bernardes, C. E. S.; da Piedade, M. E. M.; Lopes, J. N. C. *The Journal of Physical Chemistry B* **2012**, *116*, 5179–5184.

(41) Bernardes, C. E. S.; Joseph, A. *The Journal of Physical Chemistry A* **2015**, *119*, 3023–3034.

(42) Lousada, C. M.; Pinto, S. S.; Lopes, J. N. C.; da Piedade, M. F. M.; Diogo, H. P.; da Piedade, M. E. M. *The Journal of Physical Chemistry A* **2008**, *112*, 2977–2987.

(43) Ponder, J. **2011**, *3.6*.

(44) Lee, C.; Yang, W.; Parr, R. G. *Physical Review B* **1988**, *37*, 785–789.

(45) Becke, A. D. *The Journal of Chemical Physics* **1993**, *98*, 5648–5652.

(46) Lenthe, E. V.; Baerends, E. J. *Journal of Computational Chemistry* **2003**, *24*, 1142–1156.

(47) Te Velde, G.; Bickelhaupt, F. M.; Baerends, E. J.; Guerra, C. F.; van Gisbergen, S. J. A.; Snijders, J. G.; Ziegler, T. *Journal of Computational Chemistry* **2001**, *22*, 931–967.

(48) Neese, F. *Wiley Interdisciplinary Reviews: Computational Molecular Science* **2011**, *2*, 73–78.

(49) Cremer, D. *Wiley Interdisciplinary Reviews: Computational Molecular Science* **2011**, *1*, 509–530.

(50) Petersson, G. A.; Bennett, A.; Tensfeldt, T. G.; Al-Laham, M. A.; Shirley, W. A.; Mantzaris, J. *The Journal of Chemical Physics* **1988**, *89*, 2193–2218.

(51) Petersson, G. A.; Al-Laham, M. A. *The Journal of Chemical Physics* **1991**, *94*, 6081–6090.

(52) Jorgensen, W. L.; Chandrasekhar, J.; Madura, J. D.; Impey, R. W.; Klein, M. L. *The Journal of Chemical Physics* **1983**, *79*, 926–935.

(53) Frisch, M. J. et al. Gaussian˜16 Revision A.03., Gaussian Inc. Wallingford CT, 2016.

(54) Bartlett, R. J.; Musiał, M. *Reviews of Modern Physics* **2007**, *79*, 291–352.

(55) Wiberg, K. B.; Rablen, P. R. *Journal of Computational Chemistry* **1993**, *14*, 1504–1518.

(56) Berendsen, H. J. C.; Postma, J. P. M.; van Gunsteren, W. F.; DiNola, A.; Haak, J. R. *The Journal of Chemical Physics* **1984**, *81*, 3684–3690.

(57) Rogge, S.; Vanduyfhuys, L.; Ghysels, A.; Waroquier, M.; Verstraelen, T.; Maurin, G.; Speybroeck, V. V. *Journal of Chemical Theory and Computation* **2015**, *11*, 5583–5597.

(58) Humphrey, W.; Dalke, A.; Schulten, K. *Journal of Molecular Graphics* **1996**, *14*, 33–38.

(59) Meyer, J. C.; Geim, A. K.; Katsnelson, M. I.; Novoselov, K. S.; Booth, T. J.; Roth, S. *Nature* **2007**, *446*, 60–63.

(60) Lim, J.; Li, Y.; Alsem, D. H.; So, H.; Lee, S. C.; Bai, P.; Cogswell, D. A.; Liu, X.; Jin, N.; Yu, Y.-s.; Salmon, N. J.; Shapiro, D. A.; Bazant, M. Z.; Tyliszczak, T.; Chueh, W. C. *Science* **2016**, *353*, 566–571.